RSC Advances

PAPER

View Article Online
View Journal | View Issue

Open Access Article. Published on 13 May 2025. Downloaded on 12/7/2025 7:48:08 AM.
This article is licensed under a Creative Commons Attribution-NonCommercial 3.0 Unported Licence.

Check for updates

Cite this: *RSC Adv.*, 2025, **15**, 15729

Iron-doped XC-72 enhancing cobalt selenide for high-efficiency oxygen evolution reaction†

Zhiqiang Peng,[a] Hongyue Li,[a] Qile Zhou,[b] Tengfei Meng,[a] Kai Huang,[c] Chengdong Wang,[d] Peng Wang *[a] and Yupei Zhao *[a]

As an emerging class of anodic catalyst material for water electrolysis and hydrogen production, transition metal selenides exhibit excellent electron transport properties and multiphase structures with varying conductivities. However, their widespread commercial application is hindered by sluggish reaction kinetics, a lack of exposed active sites, and significant volume expansion. Cobalt, a typical transition metal element abundantly found in the Earth's crust, offers sustainability and cost-effectiveness when used as an electrode material. In this work, a series of iron-modified carbon-supported cobalt selenides exhibit excellent catalytic performance in oxygen evolution reaction (OER) testing. Among them, CS/2XC-Fe@2 demonstrates outstanding activity for the oxygen evolution reaction in 1 M KOH, achieving a current density of 10 mA cm^{-2} at a low overpotential of 261.8 mV. Additionally, density functional theory (DFT) calculations further revealed that the Fe interface with catalytic sites enhances electron transfer capabilities, as evidenced by density of states and charge analysis, which facilitates the intermediate reactions during electrocatalysis by reducing the energy barrier by 0.25 eV. This study contributes to advancing theoretical calculations and structure–activity relationship research on transition metal selenides, potentially offering a pathway for the large-scale synthesis of non-noble metal electrocatalysts.

Received 12th February 2025
Accepted 6th May 2025

DOI: 10.1039/d5ra01039j

rsc.li/rsc-advances

1. Introduction

The global demand for clean and sustainable energy is rapidly increasing, positioning water electrolysis—an efficient process that directly converts electrical energy into chemical energy—as a key technology for clean energy production.[1,2] Theoretically, the minimum voltage required for water splitting is 1.23 V; however, due to kinetic limitations, the actual operating voltage typically exceeds 1.6 V. Water electrolysis involves two half-reactions: the hydrogen evolution reaction (HER) at the cathode and the oxygen evolution reaction (OER) at the anode.[3–5] Among these, the OER, which involves a four-electron transfer, demands a higher energy input and is considered the bottleneck of the entire electrolysis process. Although noble metal oxides such as RuO_2 and IrO_2 demonstrate excellent catalytic activity in OER, their high costs restrict their widespread application in large-scale water electrolysis.[6,7] Therefore, developing efficient and cost-effective OER catalysts is crucial for advancing the industrialization of global clean energy production and expanding its applications across various fields.[8,9]

Cobalt selenide (CoSe), known for its high theoretical capacity and moderate reaction potential, has emerged as a promising candidate for OER catalysts.[10,11] However, the kinetic limitations and structural instability of CoSe result in poor rate capability and rapid capacity degradation at the anode. To address these challenges, strategies such as constructing heterostructures and engineering interfaces have been shown to enhance charge transfer and improve catalytic performance.[12–16] Ni *et al.*[17] designed a $NiSe_2/FeSe_2$ electrocatalyst through a simple selenization strategy, which exhibited exceptional OER activity, requiring only a low overpotential of 256 mV to achieve a current density of 10 mA cm^{-2}. Comprehensive analysis revealed that the well-designed built-in electric field at the heterointerface of the $NiSe_2/FeSe_2$ p–p heterojunction, resulting from energy level differences, accelerates charge transfer and enhances the conductivity of the heterostructure electrocatalyst. Xu *et al.*[18] synthesized a series of selenides, Co_x-$NiSe_y$/NF, by adjusting the Co(x) and Se(y) content. Trace Co doping induced a phase transition from hexacoordinated H–NiSe to pentacoordinated R–NiSe, forming an H–NiSe/R–NiSe heterostructure. For OER, Co_2–NiSe/NF

[a]School of Petrochemical Engineering, Changzhou University, Changzhou 213164, China

[b]Shanghai Jinyuan Senior High School, Shanghai, 200333, China

[c]Key Laboratory for Advanced Materials and Joint International Research Laboratory for Precision Chemistry and Molecular Engineering, School of Chemistry and Molecular Engineering, East China University of Science and Technology, Shanghai, 200237, China

[d]Zhenjiang Gaopeng Pharmaceutical Co., Ltd, Zhenjiang, 212006, China

† Electronic supplementary information (ESI) available. See DOI: https://doi.org/10.1039/d5ra01039j

© 2025 The Author(s). Published by the Royal Society of Chemistry

Open Access Article. Published on 13 May 2025. Downloaded on 12/7/2025 7:48:08 AM. This article is licensed under a Creative Commons Attribution-NonCommercial 3.0 Unported Licence.

achieved 1.47 V *vs.* RHE in 1.0 M KOH, approximately 30 mV lower than NiSe/NF. Zhang *et al.*[19] successfully prepared $Ni_{0.85}Se$–O/CN multinuclear core–shell heterojunction microsphere electrocatalysts *via* a simple hydrothermal method. The catalyst exhibited excellent catalytic performance at 240 mV@10 mA cm^{-2}, benefiting from the high conductivity and abundant active sites of $Ni_{0.85}Se$–O and g-C_3N_4, which synergistically overcame each other's limitations. Selenides accelerate OER kinetics through the accumulated 3d–2p repulsion between negatively charged Se sites and transition metals with optimized d-band centers, effectively facilitating oxygen release from active sites and exhibiting excellent OER activity. Li *et al.*[20] developed a composite material (($FeSe_2$ + $CoSe_2$)/N-3DCN) consisting of ultrafine and highly dispersed ($FeSe_2$ + $CoSe_2$) nanoparticles anchored on unique nitrogen-doped 3D porous ultrathin carbon nanosheets. As an efficient OER electrocatalyst, the composite benefits from the large surface area and high conductivity of the N-3DCN support, achieving an overpotential of only 312 mV at a current density of 10 mA cm^{-2}. Guo *et al.*[21] successfully grew CeO_2-coated $CoSe_2$ nanoneedles on a carbon cloth substrate. The CeO_2@$CoSe_2$/CC heterostructure exhibited a low OER overpotential of 245 mV at 10 mA cm^{-2}, with abundant oxygen vacancies in CeO_2 facilitating OH^- adsorption and accelerating the rapid conversion of $CoSe_2$ to CoOOH under low anodic voltage. He *et al.*[22] designed a sulfur vacancy-enriched Co_3S_4/MoS_2 heterostructure as a bifunctional electrocatalyst for overall water splitting. The interface and sulfur vacancies enabled fast electron transfer and enhanced electrochemical activity through synergistic effects between Co_3S_4 and MoS_2, achieving a low overpotential of 209 mV at 10 mA cm^{-2}. Meanwhile, the introduction of efficient heterointerfaces significantly enhances electron transfer, improves the intrinsic conductivity of the catalyst, and provides more reactive sites. This approach offers remarkable compositional and nanoscale structural flexibility, enabling fine-tuning of various catalytic activities, thus providing extensive options for catalyst design.

Bimetallic electrocatalysts represent a promising frontier in energy conversion and storage technologies. Compared to monometallic catalysts, bimetallic systems exhibit enhanced activity, stability, and tunability. The electronic and geometric interactions between dual metals optimize the adsorption/desorption of reaction intermediates, lowering energy barriers. Charge redistribution at bimetallic interfaces further improves intrinsic conductivity and active site exposure. For example, Yuan *et al.*[23] synthesized Fe-doped CoP hollow nanoflower clusters (Fe_2P/CoP) through templated hydrothermal reactions and high-temperature phosphidation. In alkaline media, Fe_2P/CoP achieved an OER overpotential of 269 mV at 10 mA cm^{-2}, outperforming standalone Fe_2P or CoP. Yu *et al.*[24] developed Fe-doped Co_3S_4 nanosheets directly grown on nickel foam, demonstrating efficient OER performance. These studies highlight how strategic integration of dual metals enhances catalytic efficiency by balancing electronic modulation and structural design.

To enhance the catalytic activity of cobalt selenide (CoSe) in the oxygen evolution reaction and reduce the overpotential, this study employed iron-doped XC-72 carbon as a carbon precursor to successfully synthesize iron-doped CoSe/XC-72 composite electrode materials. In OER tests, the composite material demonstrated an overpotential of 261.8 mV at a current density of 10 mA cm^{-2}, with a Tafel slope of 73.37 mV dec^{-1}, significantly outperforming pure CoSe and indicating a notable improvement in catalytic performance. Density functional theory (DFT) calculations demonstrate that the introduction of the $FeSe_2$ interface significantly enhances the conductivity and electrocatalytic performance of the CS/XC-Fe composite. DOS results reveal that the density of states near the Fermi level is substantially higher in CS/XC-Fe compared to CoSe, indicating improved electron transfer capabilities. Additionally, the D-band center shifts from −1.30 eV to −1.52 eV, suggesting weakened adsorption energy, which facilitates the desorption of reaction intermediates. Differential charge density analysis further reveals electron transfer from the $FeSe_2$ layer to the CoSe layer, with charge accumulation around Fe atoms, thereby activating Co sites and effectively improving catalytic activity. This work not merely proposes an approach for the synthesis and modification of CoSe based materials, but also provides inspirations for the design of other transition metal-based electrocatalysts.

2. Experimental

2.1 Materials

XC-72 carbon, iron acetylacetonate, and cobalt acetate tetrahydrate were purchased from Sinopharm Chemical Reagent Co., Ltd. (Shanghai, China). Selenium powder was obtained from the Chinese Academy of Metals, and a tube furnace was provided by Jingke Co., Ltd. (Anhui, China). Deionized water was used throughout the experiments.

2.2 Preparation of iron-doped XC-72 carbon

The iron-doped XC-72 carbon was synthesized using the equal-volume impregnation method. First, XC-72 carbon was activated under a CO_2 atmosphere by heating for 2 hours. After cooling, the activated XC-72 carbon was ready for further treatment. Solutions of iron acetylacetonate were prepared at different concentrations (1%, 3%, and 5% by mass). Next, 5 mL of each solution was used to impregnate the activated XC-72 carbon. The impregnated material was then heat-treated in a 5% hydrogen and 95% nitrogen atmosphere at elevated temperatures for 2 hours. After cooling, the final iron-doped XC-72 carbon material was obtained. Samples treated with different concentrations of iron acetylacetonate were labeled XC-Fe@X, where $X = 1$, 3, or 5 depending on the iron content.

2.3 Preparation of cobalt selenide/iron-doped XC-72 carbon composites

The cobalt selenide/iron-doped XC-72 carbon composite was synthesized *via* a solvothermal method. In a typical procedure, 0.1 g of selenium powder, 0.32 g of cobalt acetate tetrahydrate, 0.2 g of sodium borohydride, and the desired amount of iron-doped XC-72 carbon were added to 23 mL of ethanol. The

 © 2025 The Author(s). Published by the Royal Society of Chemistry

Open Access Article. Published on 13 May 2025. Downloaded on 12/7/2025 7:48:08 AM. This article is licensed under a Creative Commons Attribution-NonCommercial 3.0 Unported Licence.

mixture was stirred for 5 minutes to ensure complete dissolution and homogeneity. The solution was then transferred to a 50 mL Teflon-lined autoclave and heated at 180 °C for 16 hours. Upon completion of the reaction, the resulting product was washed three times with deionized water and ethanol to remove impurities. The washed material was then vacuum-dried for 8 hours to yield the cobalt selenide/iron-doped XC-72 carbon composite. To investigate the effect of varying XC-72 carbon content, samples with 0.05 g, 0.1 g, and 0.15 g of XC-72 carbon were prepared under the same conditions and labeled as CS/*y*XC-Fe@*X*, where $y = 1$, 2, or 3, corresponding to the mass of XC-72 carbon used.

2.4 Material characterization

Sample composition and crystalline properties were analyzed through X-ray diffraction (XRD, Bruker D8 advance) using Cu Kα radiation with a wavelength of 0.1541 nm. The diffraction angle ranged from 5 to 90°, with a scanning rate of $2° \cdot min^{-1}$ and a step size of 0.02°. The catalyst morphology and chemical composition were characterized using scanning electron microscopy (SEM, Nova450) and energy-dispersive X-ray spectroscopy (EDS). Further characterization of the catalyst's composition, crystal structure, and chemical composition was performed using transmission electron microscopy (TEM, JEOL JEM 2100F). X-ray photoelectron spectroscopy (XPS, Thermo Kalpha), with Al Kα radiation as the source, was employed to analyze the elemental composition and oxidation states on the catalyst's surface. All sample data were calibrated using C 1s at 284.8 eV.

3. Results and discussion

3.1 Structural and morphological characterization of the catalyst

Fig. 1(a) illustrates the preparation flowchart of CS/*y*XC-Fe@*X*. Scanning electron microscopy (SEM) observations show that CS/*y*XC-Fe@*X* exhibits a distinct particulate structure (Fig. 1(b)), which reveals an aggregated cluster-like distribution, which is beneficial for exposing more active sites. Energy-dispersive X-ray spectroscopy (EDS) images (Fig. 1(c)) confirms the homogeneous distribution of Co, Fe, and Se elements, while the C signal shows minor aggregation consistent with the carbon support's structural features. High-resolution TEM (HRTEM) images (Fig. 1(d)) further confirm the lattice spacings of CS/*y*XC-Fe@*X*, measuring 0.314 nm, 0.266 nm, and 0.185 nm, corresponding to the (100), (002), and (110) planes of CoSe.[25] These lattice spacings not only validate the XRD results but also reveal the material's crystallinity and the location of the electrocatalytic active sites.[26] Transmission electron microscopy (TEM) images (Fig. 1(e)) reveal the structure of the iron-impregnated XC-72 carbon substrate, showing a heterogeneous structure with alternating light and dark regions, which varies depending on the loading of CoSe. X-ray diffraction (XRD) patterns (Fig. 1(f)) compare the crystal structures of CS/*y*XC-Fe@*X*, CoSe, and XC-72 carbon. The XC-72 carbon shows two broad diffraction peaks at 25° and 43° in the 2θ range, characteristic of amorphous carbon, which suggests that XC-72 carbon has undergone partial graphitization after high-temperature treatment, improving its conductivity. In the XRD pattern of CS/*y*XC-Fe@*X*, three major diffraction peaks appear, corresponding to the (101), (102), and (110) planes of CoSe.[27] The (101) crystal plane is prominently exposed in the material, exhibiting high stability. Therefore, the (101) plane of CoSe was selected for further exploration in subsequent DFT calculations. Additionally, diffraction peaks at 44° and 53° are attributed to elemental iron, further confirming the successful doping of iron. The specific surface area and pore size distribution of the catalysts were tested by BET. The N_2 adsorption–desorption isotherm of CS/2XC-Fe@2 is shown in Fig. 1(g), with a specific surface area of 42.6 $m^2\ g^{-1}$ and an average pore diameter of 17.6 nm. BET results reveal that CS/2XC-Fe@2 possesses a larger specific surface area, which facilitates enhanced charge transfer.[28]

The chemical states and bonding structures of CS/2XC-Fe@2 and its individual components were investigated in detail using X-ray photoelectron spectroscopy (XPS) (Fig. 2(a), (b) and S3†). The Se XPS spectrum can be deconvoluted into two peaks, Se $3d_{5/2}$ (55.1 eV) and Se $3d_{3/2}$ (59.2 eV), confirming the presence of Se in the form of CoSe compounds.[29] The Co 2p spectrum shows split peaks due to orbital hybridization effects, where the Co $2p_{3/2}$ and Co $2p_{1/2}$ peaks correspond to Co^{3+} and Co^{2+}, further confirming the dominant valence state of cobalt in the material.[30,31] From the Fe 2p spectrum (Fig. 2(b)), the binding energies of Fe $2p_{3/2}$ and Fe $2p_{1/2}$ are observed at 711.56 eV and 725.3 eV, corresponding to Fe^{2+}, and at 714.78 eV and 728.97 eV, corresponding to Fe^{3+}.[32] The significantly higher binding energies of Fe suggest a strong electronic coupling between the XC-Fe structure and CoSe in the CS/2XC-Fe@2 heterojunction. This electronic coupling effect facilitates the injection of a small number of electrons from the XC-Fe structure to CoSe, thereby enhancing the electrocatalytic activity of cobalt. Furthermore, the full XPS spectrum of CS/2XC-Fe@2 confirms the presence of C, Fe, Co, and Se elements, consistent with the XRD and EDS analyses, comprehensively validating the composition and structure of the material. The XPS analysis not only reveals the chemical states and bonding information of each element but also provides insights into the electronic transfer mechanism within the heterojunction structure, offering key molecular-level understanding of the material's outstanding electrocatalytic performance.[33]

Furthermore, the atomic chemical states and coordination environments of Co in CS/2XC-Fe@2 were studied using X-ray absorption near-edge structure (XANES) and extended X-ray absorption fine structure (EXAFS). XANES spectra (Fig. 2(c)) show the position and shape of the absorption edge for CS/2XC-Fe@2 suggest a mixed-valence state, likely due to the interaction between cobalt and selenium, as well as contributions from iron regulating the electronic states of the system. As shown in Fourier transformed EXAFS spectra (Fig. 2(d)) for the Co foil, the introduction of the Fe-doped carbon interface endows the catalyst with a unique chemical environment. In the EXAFS spectra, CS/2XC-Fe@2 exhibits peak positions and intensities distinct from those of CoO and Co foil. This phenomenon can be attributed to the Co–Se interactions and partial charge

Open Access Article. Published on 13 May 2025. Downloaded on 12/7/2025 7:48:08 AM.
This article is licensed under a Creative Commons Attribution-NonCommercial 3.0 Unported Licence.

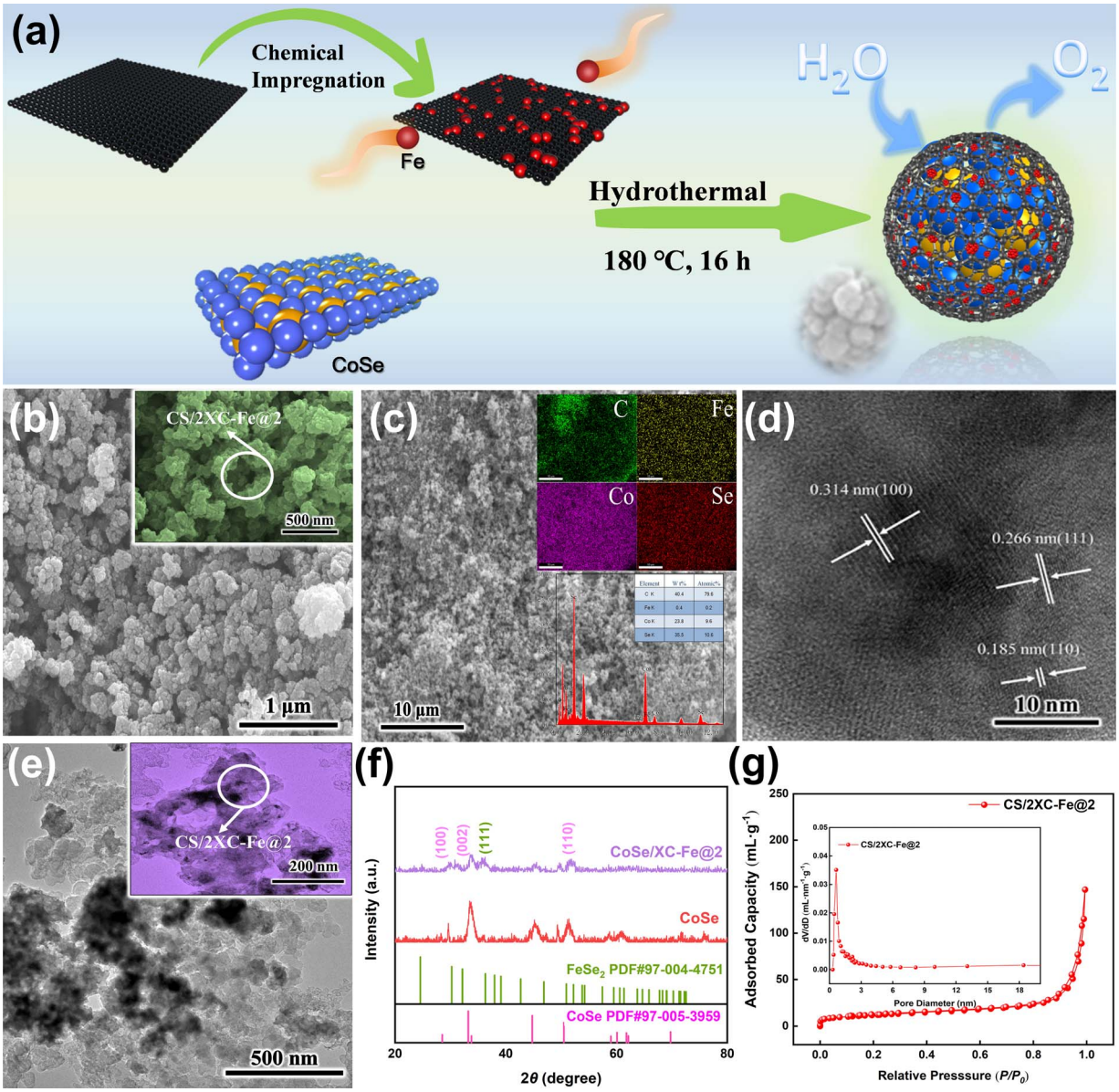

Fig. 1 (a) Schematic diagram of the preparation for CS/*y*XC-Fe@*X*, (b) SEM images of CS/2XC-Fe@1 and (c) EDS, (d) and (e) HRTEM and TEM images of CS/2XC-Fe@1, (f) XRD patterns of as-prepared CS/2XC-Fe@1, CoSe, (g) BET of CS/2XC-Fe@2.

transfer from the Fe-doped carbon interface to the CoSe interface,[34] such as reduced coordination numbers and altered bond lengths due to the incorporation of selenium and the iron-doped XC-72.

As shown in Fig. 2(e), (f) and Table 1 for CS/2XC-Fe@2, the Co–Se bond has a coordination number of 4.1 ± 0.2 and a bond length of 2.41 ± 0.004 Å, while the Co–Co bond has a coordination number of 1.9 ± 0.3 and a bond length of 2.57 ± 0.01 Å. This indicates that the Co atoms primarily interact with selenium in a higher coordination environment, with a relatively shorter bond length compared to the Co–Co interactions, which are characterized by a lower coordination number and a slightly longer bond length. The Co–Co bond length is greater than the 2.46 Å observed in Co foil, indicating weakened metallicity. The bond length of Co–Se is comparable to that of Co–O but slightly shorter, which partially reduces the electron utilization of Co. This leaves more electrons in the d-orbitals available for transfer to water, facilitating its activation. From these characterizations, it can be concluded that CS/2XC-Fe@2 possesses excellent conductivity, with electron transfer between the support and the active site significantly enhancing its catalytic activity and stability, demonstrating its potential as an efficient catalyst.

3.2 The electrochemical performance of the catalyst

The electrochemical performance of CS/*y*XC-Fe@*X* materials is shown in Fig. 3(a) and (b). The linear sweep voltammetry (LSV) curve demonstrates that CS/2XC-Fe@2 exhibits the lowest overpotential. At a current density of 10 mA cm^{-2}, the

 © 2025 The Author(s). Published by the Royal Society of Chemistry

Open Access Article. Published on 13 May 2025. Downloaded on 12/7/2025 7:48:08 AM.
This article is licensed under a Creative Commons Attribution-NonCommercial 3.0 Unported Licence.

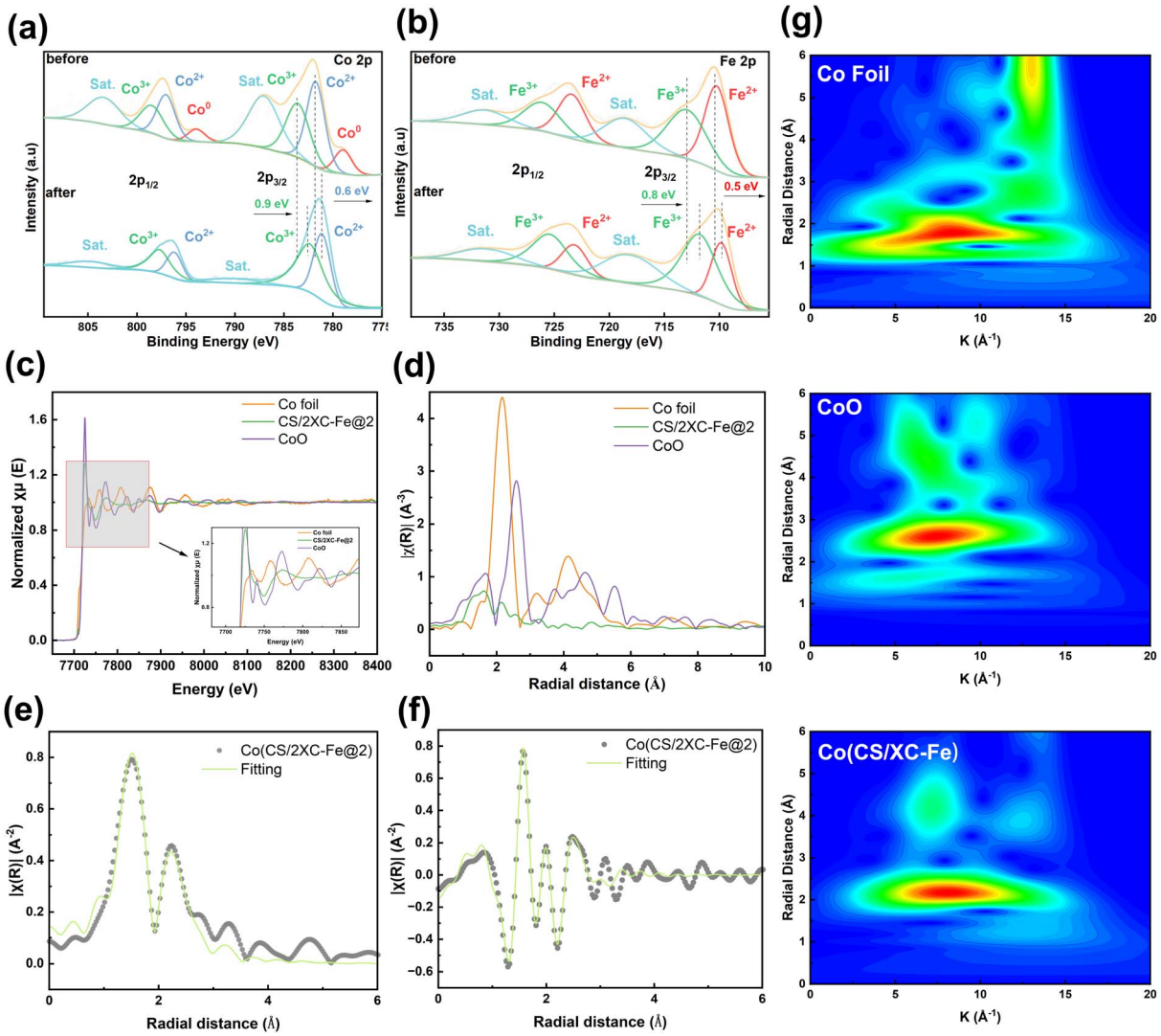

Fig. 2 (a) Co 2p, (b) Fe 2p high-resolution XPS spectra before and after OER test. (c) Co K-edge XANES spectra with Co foil and CoO as references. (d) The FT-EXAFS spectra. (e and f) Co FT-EXAFS fitting curves of CS/2XC-Fe@2. (g) WT-EXAFS spectra.

overpotential of CS/2XC-Fe@2 is 261.8 mV, whereas pure CoSe has an overpotential of 384.8 mV. This indicates that the introduction of a heterostructure significantly enhances charge transfer capabilities, enabling CS/2XC-Fe@2 to exhibit superior electrocatalytic activity in the oxygen evolution reaction. The Tafel slope is another important parameter for evaluating the electrocatalytic activity of a catalyst, as it reflects the relationship between overpotential and current density. A smaller Tafel slope indicates higher electrocatalytic activity. From the Tafel analysis (Fig. 3(c)), the Tafel slope of CS/2XC-Fe@2 is 73.37 mV dec^{-1}, which is significantly lower than the 93.35 mV dec^{-1} of CoSe. This suggests that CS/2XC-Fe@2 has superior OER reaction kinetics, with a higher reaction rate. Fig. 3(d) shows the electrochemical impedance spectroscopy (EIS) evaluation of CS/2XC-Fe@2. In general, lower electrochemical impedance values indicate easier charge transfer and faster reaction kinetics. The

Table 1 EXAFS fitting results at the Co K-edge for CS/2XC-Fe@2

Sample	Shell	CN[a]	R^b (Å)	σ^{2c} (Å^2)	$\Delta E_0{}^d$ (eV)	R Factor
Co	Co–Se	4.1 ± 0.2	2.41 ± 0.004	0.0087 ± 0.0005	−2.50	0.0173
	Co–Co	1.9 ± 0.3	2.57 ± 0.010	0.0019 ± 0.0019	−5.01	

[a] Coordination number. [b] Distance between absorber and backscatter atoms. [c] Debye–Waller factor to account for both thermal and structural disorders. [d] Inner potential correction; R factor indicates the goodness of the fit. $S_0{}^2$ was fixed to 0.95, according to the experimental EXAFS fit of Co foil by fixing CN as the known crystallographic value.

Open Access Article. Published on 13 May 2025. Downloaded on 12/7/2025 7:48:08 AM.
This article is licensed under a Creative Commons Attribution-NonCommercial 3.0 Unported Licence.

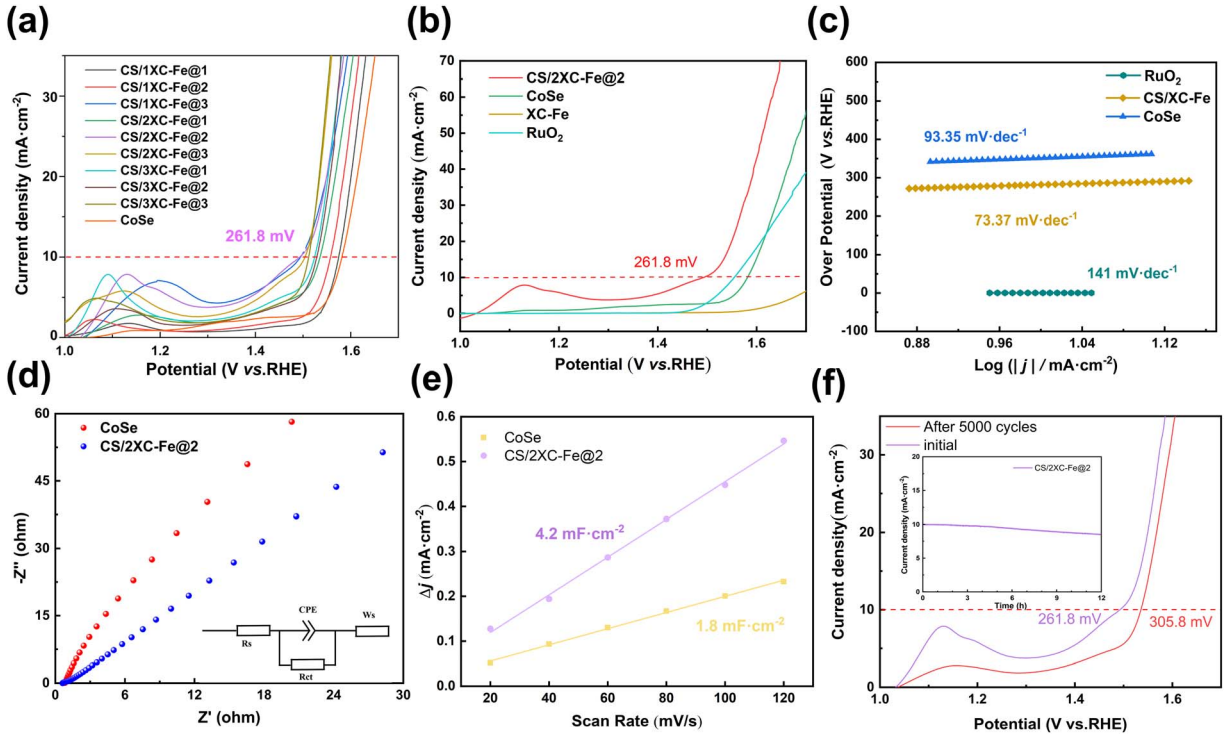

Fig. 3 (a and b) LSV curves. (c) Tafel plots. (d) Nyquist plot of 261.8 mV *vs.* RHE (for OER). (e) Double-layer capacitance. (f) The LSV curve of CS/2XC-Fe@2 after 5000 cycles (inset: the *i*–*t* curve of 10 mA cm^{-2} in OER).

results show that the charge transfer resistance of CS/2XC-Fe@2 is much lower than that of CoSe, further confirming that CS/2XC-Fe@2 facilitates more efficient charge transfer during the OER process. The C_{dl} value of CS/2XC-Fe@2 exceeds that of pure CoSe (Fig. 3(e)), indicating that CS/2XC-Fe@2 has more electrochemical active sites, which is crucial for enhancing its catalytic performance. To investigate the stability of the material, we conducted steady-state polarization tests. The results (Fig. 3(f)) show that under an initial current density of 10 mA cm^{-2}, CS/2XC-Fe@2 maintained its performance in 1 M KOH solution for 12 hours, without a significant decrease in current density. This indicates that the material has excellent stability in an alkaline medium. After 5000 cycles of CV testing, the overpotential in the LSV curve decreased by only 44.1 mV, demonstrating that CS/2XC-Fe@2 has good cyclic stability. The minor decrease in overpotential may be attributed to partial dissolution of the electrode material during cycling, but overall, the material exhibits strong stability. In summary, CS/2XC-Fe@2 demonstrates excellent electrocatalytic activity and stability in the OER, which is closely related to its optimized charge transfer properties, abundant electrochemical active sites, and superior stability.

The synergistic mechanism of the CS/2XC-Fe@2 catalyst originates from the interplay of structural and electronic factors.[35] Comparative characterization before and after reactions reveals critical insights. Iron-doped XC-72 carbon introduces $FeSe_2$ interfaces within the cobalt selenide matrix, enabling efficient electron transfer from $FeSe_2$ to CoSe. XPS analysis confirms this electronic interaction. XRD (Fig. 4(a)) and TEM results (Fig. 4(b and c)) from control experiments demonstrate a phase transition from $FeSe_2$ to FeSe alongside significant amorphous phase formation. TEM further reveals structural fragmentation, negatively impacting the long-term stability of CS/2XC-Fe@2. SEM and TEM images highlight the coral-like porous morphology of the composite, which exposes abundant active sites and enhances mass transport. Surface oxygen-containing functional groups improve hydrophilicity

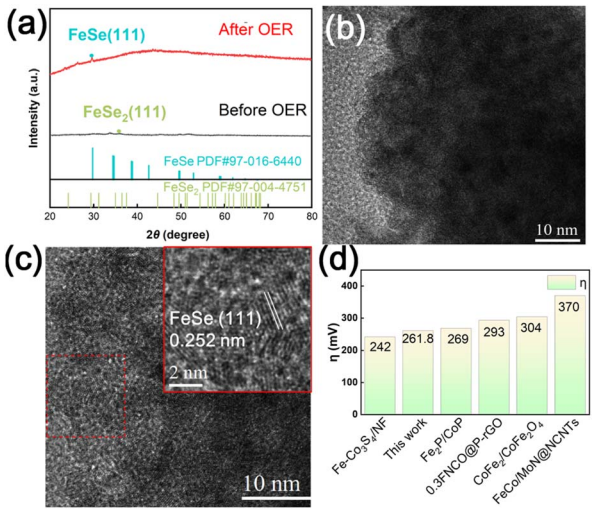

Fig. 4 (a) XRD of CS/2XC-Fe@2 after OER test, (b and c) TEM of CS/2XC-Fe@2 after OER test, (d) bimetallic site OER catalysts in recent studies.[36–38]

 © 2025 The Author(s). Published by the Royal Society of Chemistry

Open Access Article. Published on 13 May 2025. Downloaded on 12/7/2025 7:48:08 AM.
This article is licensed under a Creative Commons Attribution-NonCommercial 3.0 Unported Licence.

and intermediate adsorption. The conductive XC-72 carbon support stabilizes the heterostructure while creating a robust electron transport network. This network synergizes with the intrinsic conductivity of CoSe/$FeSe_2$, effectively minimizing charge transfer resistance. Experimental validations *via* XPS and EXAFS verify the chemical states and coordination environments of Fe and Co. Collectively, integrated interface engineering, morphology optimization, and electronic modulation drive the exceptional OER activity and stability.

3.3 DFT calculations analysis

To better elucidate the role of CoSe-based composites during the water electrolysis process, DFT calculations were conducted to investigate the surface properties and OER reaction pathway of CS/XC-Fe. XRD and TEM results revealed that the introduction of the Fe-containing interface led to the formation of a new $FeSe_2$ interface near the CoSe interface. For this heterostructure, a composite heterointerface of $FeSe_2$ and CoSe was used as a representative model. Due to the weak magnetism of CoSe and the non-magnetic nature of $FeSe_2$, spin polarization effects were not considered in this study to effectively reduce computational cost.

Fig. 5(a) and (b) present the DOS for the relevant structures. For the CS/XC-Fe composite material, the DOS near the Fermi level is significantly more abundant in CS/XC-Fe compared to CoSe, indicating enhanced conductivity and faster charge transfer rates. Moreover, calculations of the d-band center reveal that the introduction of the $FeSe_2$ interface shifts the system's d-band center from −1.30 eV to −1.52 eV. A d-band center farther from the Fermi level typically suggests that electrons tend to occupy antibonding orbitals, thereby weakening the adsorption energy. This facilitates the desorption of intermediates and reactants, promoting faster reaction kinetics.[39] Differential charge calculations were performed to construct a cross-section perpendicular to the heterojunction material. The results show that the charge transfer direction is from the $FeSe_2$ layer to the CoSe, while part of the charge accumulates around the Fe atom. After receiving electrons, Co exhibit higher catalytic activity, consistent with existing research that shows electron acquisition significantly promotes the reactivity of metals. The differential charge density map (Fig. 5(d)) reveals a significant charge transfer phenomenon between the CoSe interface and the $FeSe_2$ interface. This active interfacial electron transfer is conducive to facilitating surface catalytic reactions. This charge distribution not only enhances the conductivity of the material but also further improves the electrochemical performance of the CoSe material.[40] Fig. 5(e) shows the energy barrier and rate-determining step calculation for the OER process, following Nørskov's classic four-electron theory.[41] The overall free energy change for the OER process is 4.92 eV, which is consistent with the widely accepted results. Fig. 5(f) illustrates the energy pathway for the OER process, indicating that the rate-determining step for the CoSe/$FeSe_2$ heterojunction in the OER process is the conversion of adsorbed *OH to *O. Additionally, the adsorption of OH on a catalyst surface which has

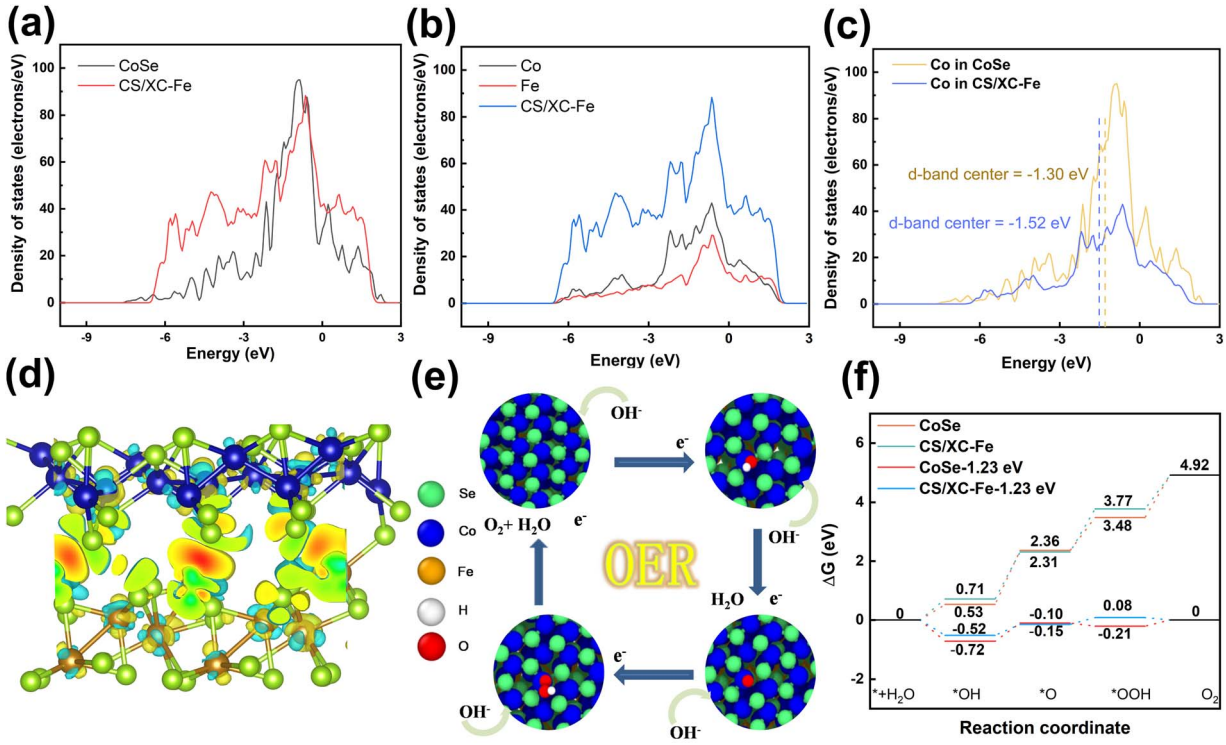

Fig. 5 (a) Total density of states of CoSe and CS/XC-Fe, (b) PDOS of CS/XC-Fe, (c) DOS of CoSe (where the line represents the D-band center position), (d) difference charge density distribution of CS/XC-Fe, (e) schematic diagram of different intermediates during the OER process of CS/XC-Fe, (f) energy pathway diagram of the OER process for CoSe and CS/XC-Fe.

Open Access Article. Published on 13 May 2025. Downloaded on 12/7/2025 7:48:08 AM.
This article is licensed under a Creative Commons Attribution-NonCommercial 3.0 Unported Licence.

already adsorbed O also requires a relatively low energy, while the adsorption of OH followed by dehydrogenation to form adsorbed O is relatively harder. The overall energy barrier for the process is 1.6 eV. Under a certain applied voltage, the influence of the $FeSe_2$ interface reduces the energy barrier of the rate-determining step for OER intermediates on CS/XC-Fe to only 0.37 eV, which is significantly lower than the 0.62 eV observed for CoSe.

4. Conclusions

In summary, a $FeSe_2$ interface was introduced at the cobalt selenide interface through pyrolysis and a hydrothermal method. This material exhibits a unique coral-like morphological structure, providing a large number of active sites. Characterization analysis reveals the presence of oxygen-containing groups on the surface of the material, which play a positive role in enhancing the electrochemical activity. Electrochemical performance tests indicate that, at a current density of 10 mA cm^{-2}, the overpotential for the oxygen evolution reaction of the CS/2XC-Fe@2 material is 261.8 mV, with a Tafel slope of 73.37 mV dec^{-1}. Compared to pure CoSe, CS/2XC-Fe@2 demonstrates superior electrochemical activity, primarily attributed to its unique structure and the electronic structure modulation induced by iron doping. This study highlights the importance of structural engineering and metal doping in optimizing the electrochemical performance of catalytic materials. The findings provide new insights into how iron doping can significantly modulate the electronic structure of cobalt selenide, enhancing its catalytic properties. This approach of tuning the d-band center through metal doping offers a valuable strategy for the design of highly efficient, low-cost catalysts for OER and other related electrochemical processes. The theoretical calculations further deepen the understanding of the catalytic mechanism, particularly by identifying how iron doping influences the rate-determining step of the OER process. These insights contribute to understanding the structure–performance relationship of transition metal selenides, facilitating the exploration of their catalytic sites and electrochemical performance through experimental or computational techniques.

Data availability

The data supporting this article have been included as part of the ESI.†

Author contributions

Zhiqiang Peng: Conceptualization, data curation, formal analysis, writing – original draft. Hongyue Li: Investigation, validation, visualization. Qile Zhou: Data curation. Tengfei Meng: Investigation, validation. Kai Huang: Data curation, software. Chengdong Wang: Writing – review & editing, funding acquisition. Peng Wang: Supervision, validation, writing – review & editing, funding acquisition. Yupei Zhao: Conceptualization, funding acquisition, resources, supervision, project administration, writing – review & editing.

Conflicts of interest

The authors declare that they have no conflict of interest.

Acknowledgements

The authors are grateful for financial support from the National Natural Science Foundation of China (No. 22072007), Natural Science Foundation of Jiangsu Province (BK20231239), Jiangsu Graduate Research and Practice Innovation Program (No. KYCX23_3115, No. SJCX23_1523), Zhenjiang Key Research and Development Program (Industry Foresight and Common Key Technologies, No. CQ2022006), and the Jiangsu Graduate Workstation. We also thank the Anhui Absorption Spectroscopy Analysis Instrument Co., Ltd. for XAFS measurements and analysis.

References

1 S. Klemenz, A. Stegmüller, S. Yoon, C. Felser, H. Tüysüz and A. Weidenkaff, *Angew. Chem., Int. Ed.*, 2021, **60**, 20094–20100.
2 M. Blasco-Ahicart, J. Soriano-López, J. J. Carbó, J. M. Poblet and J. R. Galan-Mascaros, *Nat. Chem.*, 2018, **10**, 24–30.
3 J. Wang, W. Liu, G. Luo, Z. Li, C. Zhao, H. Zhang, M. Zhu, Q. Xu, X. Wang, C. Zhao, Y. Qu, Z. Yang, T. Yao, Y. Li, Y. Lin, Y. Wu and Y. Li, *Energy Environ. Sci.*, 2018, **11**, 3375–3379.
4 J.-Y. Park, J. A. Rajesh, S.-H. Kang and K.-S. Ahn, *J. Alloys Compd.*, 2023, **951**, 169979.
5 Z. Li, M. Hu, P. Wang, J. Liu, J. Yao and C. Li, *Coord. Chem. Rev.*, 2021, **439**, 213953.
6 B. Deng, J. Liang, L. Yue, T. Li, Q. Liu, Y. Liu, S. Gao, A. A. Alshehri, K. A. Alzahrani, Y. Luo and X. Sun, *Chin. Chem. Lett.*, 2022, **33**, 890–892.
7 Y. Wu, Y. Zhang, M. V. Nguyen, T. T. H. Chu, T. B. H. Nguyen, E.-N. Dragoi and C. Xia, *Mol. Catal.*, 2023, **534**, 112818.
8 Y. Hu, Y. Zheng, J. Jin, Y. Wang, Y. Peng, J. Yin, W. Shen, Y. Hou, L. Zhu, L. An, M. Lu, P. Xi and C.-H. Yan, *Nat. Commun.*, 2023, **14**, 1949.
9 Y. Gao, N. Zhang, C. Wang, F. Zhao and Y. Yu, *ACS Appl. Energy Mater.*, 2020, **3**, 666–674.
10 M. Basu, Z.-W. Zhang, C.-J. Chen, T.-H. Lu, S.-F. Hu and R.-S. Liu, *ACS Appl. Mater. Interfaces*, 2016, **8**, 26690–26696.
11 C. A. Campos-Roldán and N. Alonso-Vante, *J. Electrochem. Soc.*, 2020, **167**, 026507.
12 M. Chen, Y. Hu, K. Liang, Z. Zhao, Y. Luo, S. Luo and J. Ma, *Nanoscale*, 2021, **13**, 18763–18772.
13 Y. Wu, F. Wang, N. Ke, B. Dong, A. Huang, C. Tan, L. Yin, X. Xu, L. Hao, Y. Xian and S. Agathopoulos, *J. Alloys Compd.*, 2022, **925**, 166683.
14 M. Hao, H. Wang, X. Zhang, Y. Qu, C. Xuan, Z. Wu, M. Cui and J. Wang, *New J. Chem.*, 2022, **46**, 8250–8255.
15 J. Yu, Y. Cao, Q. Liu, Y. Luo, Y. Liu, X. Shi, A. M. Asiri, T. Li and X. Sun, *ChemNanoMat*, 2021, **7**, 906–909.

 © 2025 The Author(s). Published by the Royal Society of Chemistry

Open Access Article. Published on 13 May 2025. Downloaded on 12/7/2025 7:48:08 AM.
This article is licensed under a Creative Commons Attribution-NonCommercial 3.0 Unported Licence.

16 K. Dang, S. Zhang, X. Wang, W. Sun, L. Wang, Y. Tian and S. Zhan, *Nano Res.*, 2021, **14**, 4848–4856.
17 S. Ni, H. Qu, Z. Xu, X. Zhu, H. Xing, L. Wang, J. Yu, H. Liu, C. Chen and L. Yang, *Appl. Catal., B*, 2021, **299**, 120638.
18 J. Xu, J. Ruan, Y. Jian, J. Lao, Z. Li, F. Xie, Y. Jin, X. Yu, M.-H. Lee, Z. Wang, N. Wang and H. Meng, *Small*, 2024, **20**, 2305905.
19 C. Zhang, W. Xu, S. Li, X. Wang, Z. Guan, M. Zhang, J. Wu, X. Ma, M. Wu and Y. Qi, *Chem. Eng. J.*, 2023, **454**, 140291.
20 H. Li, H. Xie, X. Wang, E. Liu, J. Kang, C. Shi, J. Sha and L. Ma, *ACS Appl. Nano Mater.*, 2023, **6**, 9598–9607.
21 Q. Guo, Y. Li, Z. Xu and R. Liu, *Adv. Energy Mater.*, 2025, **15**, 2403744.
22 Q. He, N. Ye, L. Han and K. Tao, *Inorg. Chem.*, 2023, **62**, 21240–21246.
23 Y. Yuan, Y. Yang, H. Xie, X. Zhong, R. Wang and Z. Xu, *Int. J. Hydrogen Energy*, 2024, **90**, 1401–1410.
24 J. Yu, M. Gao, Y. Si, L. Chen and P. Zhang, *Mater. Lett.*, 2023, **353**, 135242.
25 L. Zhang, J. Guo, M. Yuan, Y. Xu, Z. Pu, C. Tan, Q. Wang and X. Xiong, *Anal. Chim. Acta*, 2024, **1329**, 343236.
26 X. Xing, C. Wu, G. Yang, T. Tong, Y. Wang, D. Wang, F. C. Robles Hernandez, Z. Ren, Z. Wang and J. Bao, *Mater. Today Chem.*, 2022, **26**, 101110.
27 H. Liang, L. Jia, F. Chen, S. Jing and P. Tsiakaras, *Appl. Catal., B*, 2022, **317**, 121698.
28 Z. Y. Huang, Y. F. Yuan, Z. J. Yao, M. Zhu, S. M. Yin, Y. Z. Huang, S. Y. Guo and W. W. Yan, *Appl. Surf. Sci.*, 2023, **637**, 157886.
29 X. Wang, Y. Zhou, M. Liu, C. Chen and J. Zhang, *Electrochim. Acta*, 2019, **297**, 197–205.
30 C. Deng, L. Yang, C. Yang, P. Shen, L. Zhao, Z. Wang, C. Wang, J. Li and D. Qian, *Appl. Surf. Sci.*, 2018, **428**, 148–153.
31 S. Liu, K. Feng, W. Xu, X. Shi, Z. Xu and C. Wang, *Colloids Surf., A*, 2024, **680**, 132711.
32 J. Chen, L. Li, Y. Cheng, Y. Huang and C. Chen, *Int. J. Hydrogen Energy*, 2022, **47**, 16025–16035.
33 Y. Wang, Y. Yang, X. Wang, P. Li, H. Shao, T. Li, H. Liu, Q. Zheng, J. Hu, L. Duan, C. Hu and J. Liu, *Nanoscale Adv.*, 2020, **2**, 792–797.
34 Y. Zhou, J. Zhang, H. Ren, Y. Pan, Y. Yan, F. Sun, X. Wang, S. Wang and J. Zhang, *Appl. Catal., B*, 2020, **268**, 118467.
35 M. Al-Rasheidi, F. Khan, M. Y. Khan, A. Khan and M. T. Khan, *Int. J. Hydrogen Energy*, 2024, **93**, 1502–1511.
36 S. Sarkar, P. Chaubey and P. K. Sharma, *J. Alloys Compd.*, 2025, **1010**, 177856.
37 R. A. Raimundo, V. D. Silva, L. S. Ferreira, F. J. A. Loureiro, D. P. Fagg, D. A. Macedo, U. U. Gomes, R. M. Gomes, M. M. Soares and M. A. Morales, *J. Alloys Compd.*, 2023, **940**, 168783.
38 Y. Zhang, W. Xue, Y. Ding, J. Chen and X. Xu, *Inorg. Chem. Commun.*, 2025, **177**, 114374.
39 Y. Jiang, P. Sun, L. Sharma, B. Mao, R. Kakkar, T. Meng, L. Zheng and M. Cao, *Nano Energy*, 2021, **81**, 105645.
40 A. Meena, P. Thangavel, A. S. Nissimagoudar, A. Narayan Singh, A. Jana, D. Sol Jeong, H. Im and K. S. Kim, *Chem. Eng. J.*, 2022, **430**, 132623.
41 J. K. Nørskov, J. Rossmeisl, A. Logadottir, L. Lindqvist, J. R. Kitchin, T. Bligaard and H. Jónsson, *J. Phys. Chem. B*, 2004, **108**, 17886–17892.

© 2025 The Author(s). Published by the Royal Society of Chemistry